Method for spike detection from microelectrode array recordings contaminated by artifacts of simultaneous two-photon imaging

Gábor Orbán[1,2]*, **Domokos Meszéna**[2,3]**, Kinga Réka Tasnády**[2]**, Balázs Rózsa**[3,4]**, István Ulbert**[3]**, Gergely Márton**[1,2,3]

1 Doctoral School on Materials Sciences and Technologies, Óbuda University, Budapest, Hungary, **2** Institute of Cognitive Neuroscience and Psychology, Research Centre for Natural Sciences, Hungarian Academy of Sciences, Budapest, Hungary, **3** Faculty of Information Technology and Bionics, Pázmány Péter Catholic University, Budapest, Hungary, **4** Institute of Experimental Medicine, Hungarian Academy of Sciences, Budapest, Hungary

* orban.gabor@ttk.mta.hu

Abstract

The simultaneous utilization of electrophysiological recordings and two-photon imaging allows the observation of neural activity in a high temporal and spatial resolution at the same time. The three dimensional monitoring of morphological features near the microelectrode array makes the observation more precise and complex. In vitro experiments were performed on mice neocortical slices expressing the GCaMP6 genetically encoded calcium indicator for monitoring the neural activity with two-photon microscopy around the implanted microelectrodes. A special filtering algorithm was used for data analysis to eliminate the artefacts caused by the imaging laser. Utilization of a special filtering algorithm allowed us to detect and sort single unit activities from simultaneous two-photon imaging and electrophysiological measurement.

Introduction

Measurement methods which yield signals of neural activities with high information content, such as electrocorticography (ECoG) and intracortically implanted high density microelectrode arrays (MEAs), have vastly contributed to the progress of neuroscience and brain-computer interfacing [1–4]. MEAs are not only capable of recording the summed bioelectrical activities of neuron populations (i.e. local field potentials, LFPs), but they can also detect individual activities of neurons (i.e. single unit activities, SUAs) [5,6]. These methods had an instrumental role in the functional mapping of the brain [7] and they are still the ultimate solution when high spatial and temporal resolution are required [4,8,9]. However, the spatial range of the SUA detection capability of the implanted sensors is limited to the immediate surroundings the electrode sites, i.e. hundred micron wide volumes [10]. Furthermore, the long term use of implanted MEAs is corrupted by the degradation of their performance over weeks or

Competing interests: The authors have declared that no competing interests exist.

months, let alone years [11–13]. The underlying causes range from material failures [14,15] to the deteriorative effects of the immune response to the implants [16–18].

In the last few decades, various optical imaging methods became widely used in neuroscience, which can render wide brain regions observable with high spatial resolution [19–23]. Furthermore, the application of two-photon microscopy with fluorescent calcium indicators makes the monitoring of neural activity (e.g. action potentials of individual cells) possible [24–27]. The focal length of fluorescence microscope objectives can exceed 12 mm [28], which allows the implantation of depth MEAs into the optical cranial window [29].

Simultaneous application of depth MEAs for extracellular electrophysiology and two-photon imaging could allow neuroscientists to observe activities of individual neurons with good spatial and temporal resolution at the same time, thus the more precise and complex pieces of information could be obtained from neural activity [30]. The extension of high density intracortical recordings with simultaneous two-photon microscopy would enable three dimensional optical monitoring of the structural features of the cells located close to the electrode.

Nonetheless, the co-localized and simultaneous application of two-photon imaging and electrophysiological measurement by MEAs remains challenging, partly because of the photoelectric artefacts on the electrophysiological recordings caused by the imaging laser [31]. The artefacts generally appear as huge sawtooth-like waves. The main frequency of such waves correspond to the imaging frame rate of the applied two-photon laser. The frame rate of the imaging is indeterminate, moreover, the sharp shape of the waves and other effects introduce various harmonics other than the main frequency, thus elimination of the photoelectric artefacts requires more subtle methods than applying e.g. a notch filter. Comb filters have already been successfully used for decreasing stimulus artefacts [32] and 50 Hz low frequency noise [33] from electrophysiological signals, while adaptive filters are utilized e.g. in brain-computer interface development [34,35], in simultaneous measurements of real-time magnetic resonance imaging and electrocardiogram recordings [36], in fetal electrocardiogram analysis [37], etc.

In this study we present a method wherein the utilization of a custom-set comb filter based algorithm allowed us to detect and sort SUAs from extracellular multi-channel recordings while the measuring electrode array and the surrounding tissue was monitored with two-photon imaging. The method was validated by applying the filter on recording sections when the imaging laser was not in use and checking whether the introduced laser artefact affects SUA detection and clustering.

Materials and methods

Preparation of in vitro experiments

In vitro experiments were performed on mice expressing the GCaMP6 genetically encoded calcium indicator for the monitoring of neural activity around the MEA [38,39].

A total of three GCaMP mice had been anesthetized with a ketamine-xylazine solution and prepared for operation as described elsewhere [40]. Animals for acute tests were kept and handled in accordance with the European Council Directive of 24 November 1986 (86/609/EEC), the Hungarian Animal Act, 1998 and the Animal Care Regulations of the Research Centre for Natural Sciences of the Hungarian Academy of Sciences (RCNS-HAS). The study was approved by the Institutional Animal Care and Use Committee of the Research Centre for Natural Sciences of the Hungarian Academy of Sciences (members: Dr. István Ulbert, Dr. József Topál and Péter Kottra) and the National Food Chain Safety Office of Hungary (PEI/001/695-9/2015). Animals had unlimited access to food and water, when they were awake. Each mouse was kept in a 39 cm long, 22 cm wide, 18 cm high cage. They were under deep

anesthesia during surgery as well as at the time of sacrifice. Efforts were made to minimize animal suffering and to reduce the number of animals used.

Cortical and hippocampal slices were prepared from the mice brains. The brains were immediately removed and dipped into cold (2–3˚C), oxygenated (95% O_2, 5% CO_2) cutting solution. The cutting solution contained the following composition (in mM): 250 Sucrose, 26 $NaHCO_3$, 10 D-Glucose, 1 KCl, 1 $CaCl_2$ and 10 $MgCl_2$. 500 μm-thick horizontal slices were cut by a vibratome (VT1200s; Leica, Nussloch, Germany) from both hemispheres. Slices were kept in a standard artificial cerebrospinal fluid (aCSF) solution at room temperature (20–22˚C) for at least 1 hour before use. The recordings were performed at 32–34˚C with a standard recording aCSF containing (in mM): 124 NaCl, 26 $NaHCO_3$, 10 D-Glucose, 4 KCl, 2 $CaCl_2$ and 2 $MgCl_2$. In the recording chamber, a dual-perfusion system was used by perfusing both the top and the bottom surfaces of the slices with relatively high perfusion speed (>10 ml/min) to provide better oxygenation, similar to in vivo conditions [41].

Two-photon imaging

The three dimensional observation of morphology was performed with two-photon microscope (Femtonics Ltd., Budapest, Hungary). The two-photon imaging not only let us monitor the neural activity near the applied MEA because of the genetically encoded calcium indicator expressing GCaMP6 cells, but it also made the observation of imaging laser generated artefacts possible. For the optical imaging the prepared slices were placed into an in vitro measuring chamber. The chamber ensured the aCSF supplement and circulation for keeping the neural tissue alive until the end of the measurement and it stabilized the slice mechanically with a holder mesh. The top part of the chamber is concave-shaped to hold the aCSF for the liquid immersion objective of the two-photon microscope which was used during the experiments. The applied laser had a wavelength of 940 nm and worked in resonant mode.

The setup was not only able to function in two-photon imaging mode but it also did work in camera mode which allowed us to follow the track of the inserted MEA before and during the insertion because of the built-in CCD camera. With the brain slice in place, the bioelectrical activity was monitored in two-photon mode and the electrophysiological measurement setup was assembled.

Electrophysiological measurement

The electrophysiological observation of the bioelectrical activity of the examined brain slices were carried out using an Intan RHD—2000 amplifier system (Intan Technologies LLC., Los Angeles, CA, USA) connected to a computer via USB 2.0 with a sampling frequency of 20 kHz. The reference electrode was an Ag/AgCl needle located beneath the tested brain slice. A MEA with 16 shanks (1 electrode/shank) (A16x1-2mm-50-177-A16, NeuroNexus, Ann Arbor, MI. USA) was employed as a working electrode. The MEA was attached to one of the automated electrode holder of the two-photon setup in such a manner that the longitudinal axes of the shanks included an angle of 30 degrees relative to the surface of the brain slice. The implantation was performed under CCD camera control. After the MEA had reached its final place in the tissue, the two-photon setup was switched from camera mode to two-photon mode and the electrode sites were located. The schematic of the assembled experiments is shown in Fig 1. Following this, the focal plane was stabilized and the imaging laser was turned off. The electrophysiological measurement was started without the laser in order to provide reference recordings. After 8 minutes of such laser-free recordings, the two-photon imaging was initiated and the imaging laser introduced artefacts. Another 8 minutes of laser-noised recordings were hence obtained. The third part of each measurement was performed without the two-
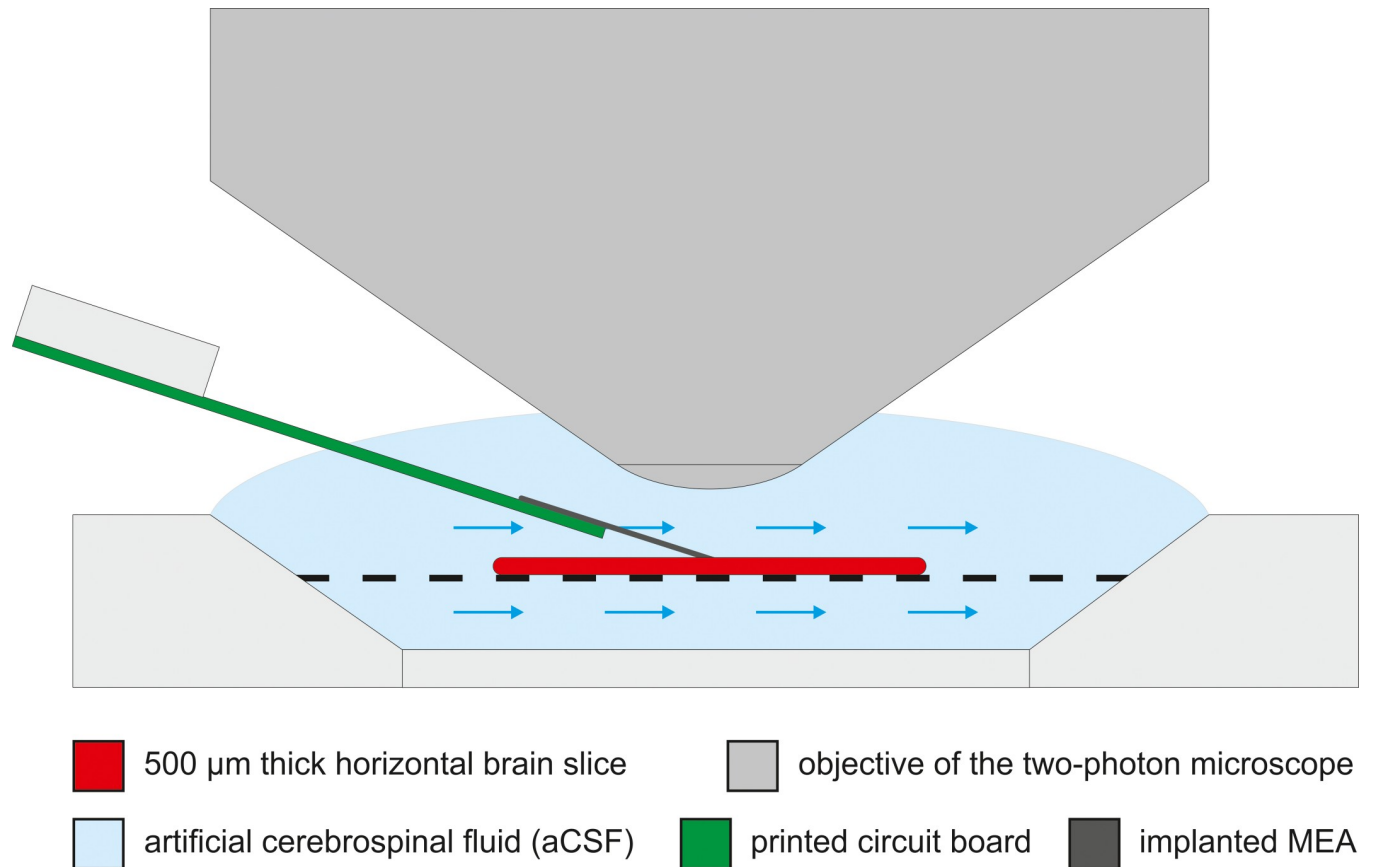
Fig 1. Schematic of the assembled measuring system. In the middle of the in vitro two-photon measuring chamber the brain slice is placed on a holder mesh. The chamber provides the aCSF circulation near the neural tissue to keep it bioelectrically active. Under the fluid immersed two-photon objective the applied MEA was inserted into the tissue.

photon imaging again, in order to obtain further control data sessions, this time after the laser effect. During the second part of the measurements, the laser generated artefacts which exceeded the amplitude of SUAs by at least an order of magnitude (Fig 2).

Data analysis

MATLAB 2017a (MathWorks Inc., Natick, MA, USA) was used for off-line signal visualization, filtering and analysis. Fig 3 summarizes the steps that had been performed in order to accomplish our ultimate goal, i.e. the identification of spike clusters in the data containing two-photon laser noise.

All of the applied band-stop IIR filters were created with passband ripples of 0.4. Since the IIR filters delay some frequency components more the others, they distort the input signals with frequency dependent phase shift. Thus they were applied with the 'filtfilt' Matlab function that compensated the delays introduced by such filters, and thus corrected for filter distortion. The recorded signals were initially filtered with a second order band-pass filter between 300 Hz and 3000 Hz, which is a commonly used method for highlighting and detecting SUAs [42], but not adequate for eliminating the photoelectric artefacts. Following this, Fast Fourier transform (FFT) was applied on the electrophysiological recordings. Comparing the frequency spectra of the first (laser off) part of each measurement to their second part (laser on), it was evident that the imaging laser gave rise to a population of high peaks in the frequency domain.
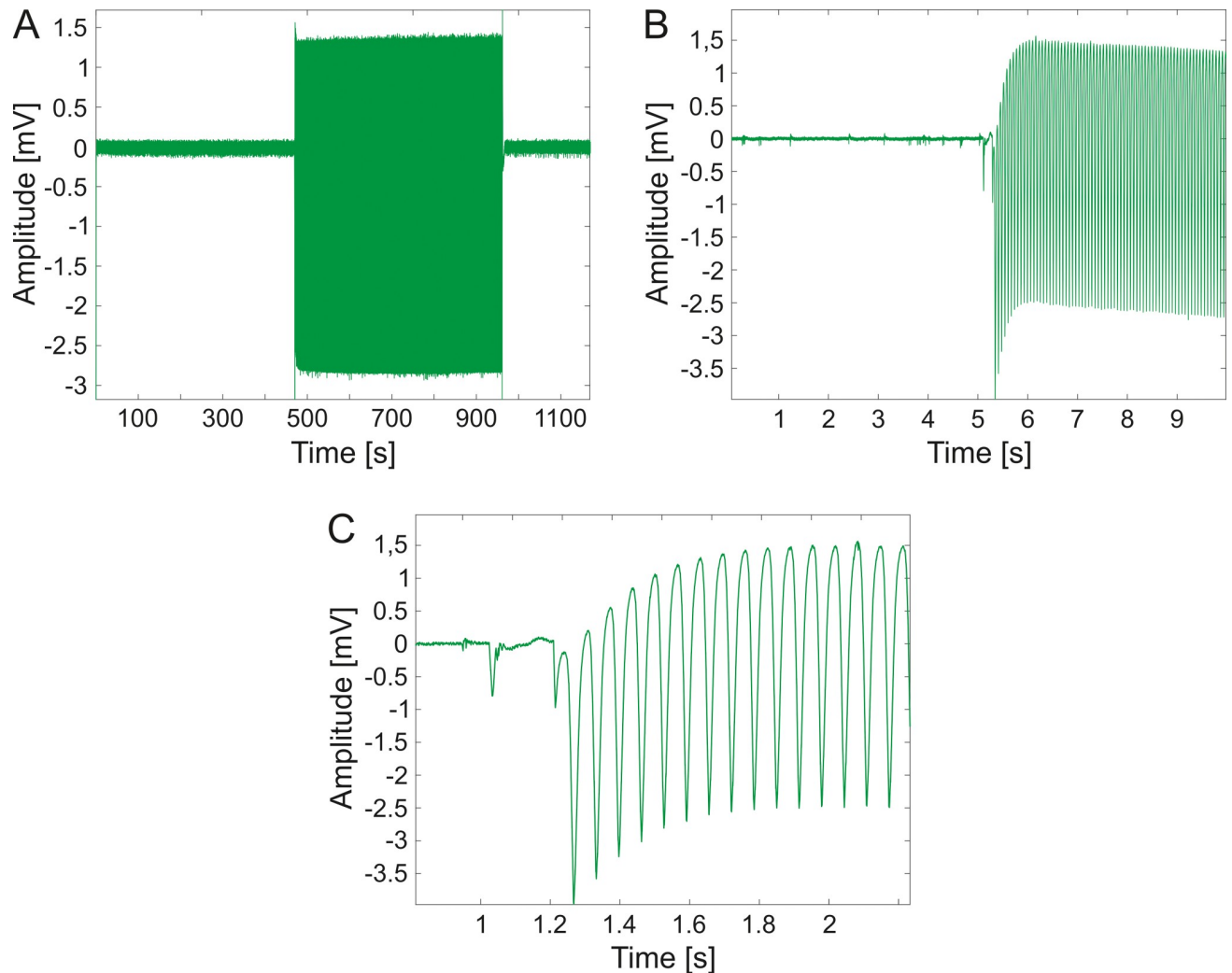
Fig 2. Representative sample of the imaging laser impact on the electrophysiological recordings. Between the first and the last parts of the measurement, which were recorded without two-photon imaging, photoelectric artefacts of the two-photon imaging laser are observable (A). The recorded data at the moment when the imaging laser was switched on (B, C).

These peaks were located periodically, with a distance of 15.5 Hz between the neighboring ones. This frequency value corresponds to the imaging frame rate of the applied two-photon laser (Fig 4). Considering this nature of the artefacts, it is a straightforward idea to utilize of a comb filter algorithm to eliminate the noise of the imaging laser. Fig 3 shows the whole data evaluation process for spike sorting (Fig 3A), including the construction of the laser noise reduction filters (Fig 3B). Such a comb filter had to be constructed individually for every recording channel because of the different laser noise characteristics on the channels. Each custom-set comb filter was built from filter modules, a representative filter module is shown in Fig 3C. The modules contain band-stop filters fitted to a certain amount of peaks in the frequency domain.

The parameter setting algorithm of the comb filter is shown in Fig 3B. These parameters were the number of filter modules (N_M), a vector containing the center frequencies of the filter modules (f_{peak}), the numbers of the applied band-stop filters within each module (N_F) and the distances between the center frequencies of the applied band-stop filters within each module (D_F). The parameter setting algorithm utilized the 300–3000 Hz filtered laser noisy data in a
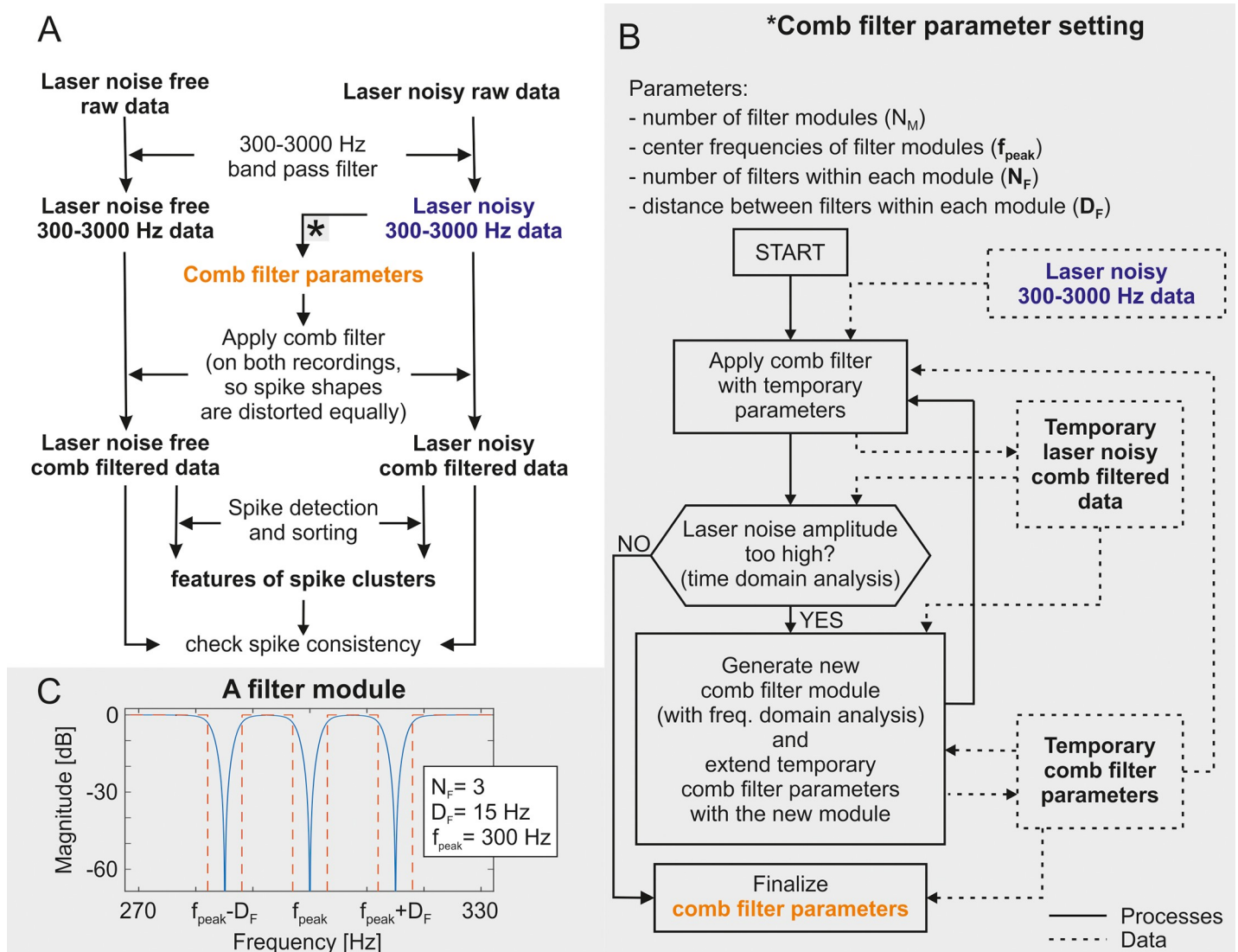
Fig 3. Filtering and analyzing steps. The performed filtering and analyzing steps in order to identify the spike clusters and check the spike consistency between the two-photon imaging laser noise free and the laser noisy data (A), the parameter setting algorithm of the applied custom-set comb filter (B) and the result of the parameter setting of a representative filter module (C).

cyclic manner, during each cycle, a new filter module is added to the comb filter. The first step in the cycle was the generation of a temporary laser noise filtered data by the application of the temporary comb filter, i.e. the comb filter generated in the previous cycle on the 300–3000 Hz filtered laser noisy data (in the first cycle the number of filter modules is 0, so this step left the data unchanged). The second step was deciding whether the temporary filter was sufficient. This was performed by time domain analysis on the temporary laser noisy filtered data. If the amplitude of the periodic laser noise had been reduced below 40 µV, then the temporary filter parameters became the finalized comb filter parameters. Otherwise, the last step in the cycle followed, which was the generation of a new filter module. This was performed based on the frequency domain analysis of the temporary laser noisy comb filtered data (which is equivalent to the 300–3000 Hz filtered laser noisy data in the first step). After applying the FFT on this data, the algorithm found the highest peak in the frequency domain. This frequency became
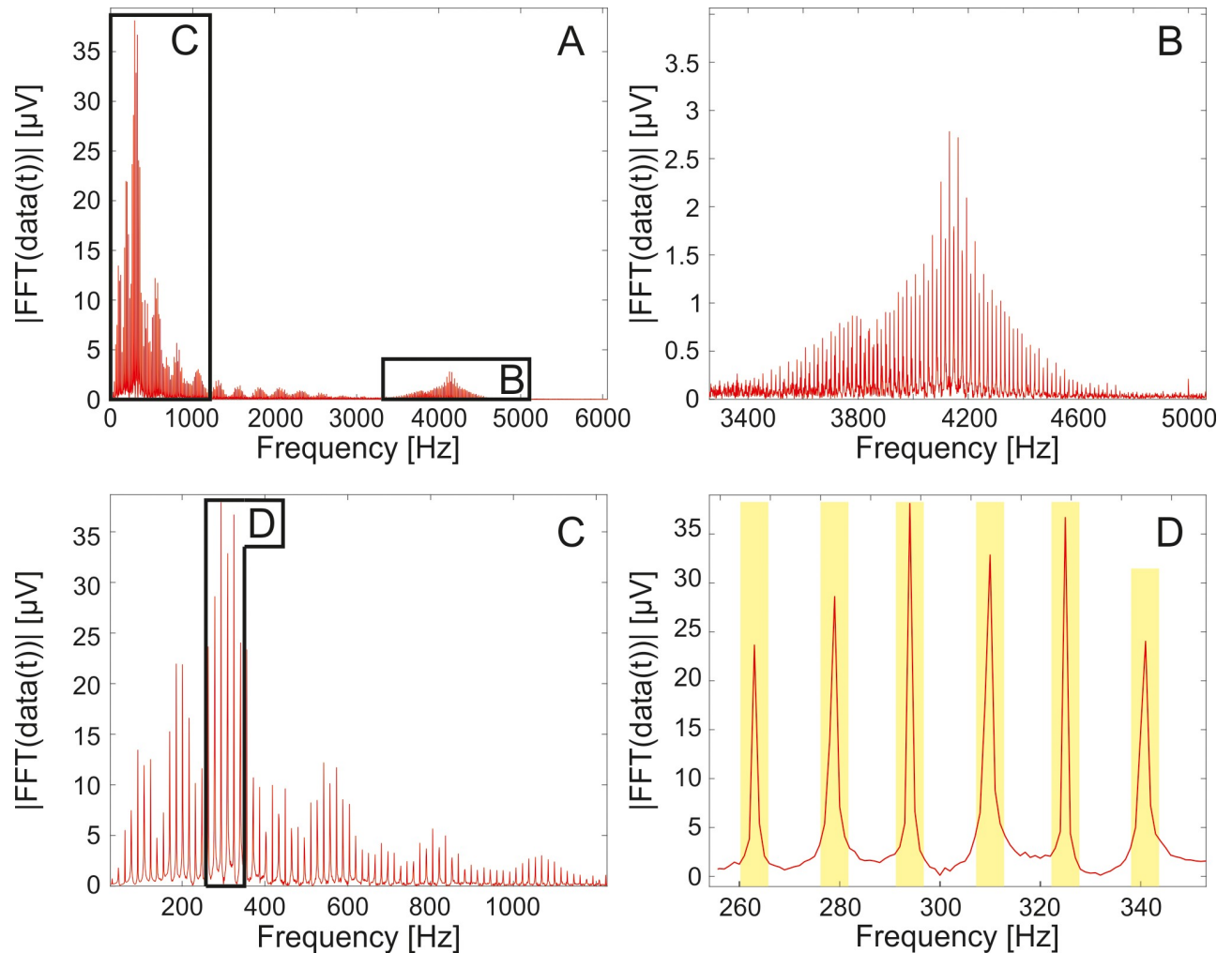
Fig 4. The absolute value of the frequency spectrum of the electrophysiological recordings. The fast Fourier transform analysis of the imaging laser generated noise in the electrophysiological recorded data (A). Harmonics below 1200 Hz (C) and at higher frequencies (B) of the laser generated periodical artefacts appeared with high magnitudes. The overlap of the harmonics is observable (B). A part of the rejected frequencies by the custom-set comb filter is shown in yellow (D).

the center frequency (f_{peak}) of the new filter module. The neighboring peaks were located at the frequencies of $f_{peak} \pm n \cdot D_F$ (D_F was found to be 15.5 Hz). The values at the neighboring peaks were compared to the highest detected peak to define the number of the applied filters (N_F) within the new module. N_F of the filter module was defined so that the band-stop filters of the comb filter would cover all the neighboring peaks which exceeded in height the 15% of the highest peak (i.e. the one at the center frequency). Every band-stop filter element of the new comb filter module was defined with cutoff frequencies at below 3 Hz and above 3 Hz from the frequency value of each peak. Thus the central rejected frequencies of the comb filter were adjusted to the frequencies of the laser noise peaks and each section of the comb filter had a 6 Hz wide rejected band, as shown in Fig 3C and in Fig 4D. The temporary comb filter was extended with the thus obtained new module and the cycle restarted. This process was repeated until the time domain analysis gave positive result, i.e. the amplitude of the laser noise peaks in the time domain became lower than 40 μV, in which case the summarized comb filter parameters were accepted.
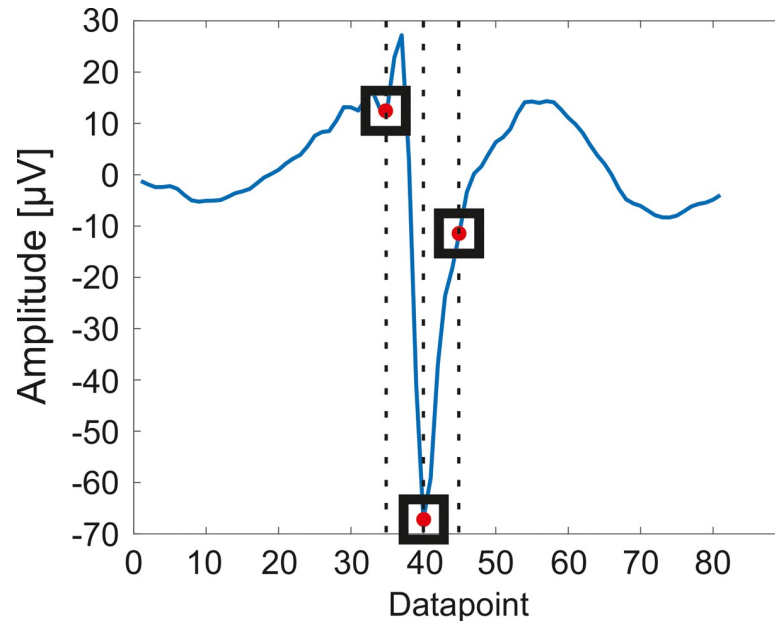
Fig 5. The applied principal component selection. Each potential spike was defined with their three principal component before spike sorting: the location of the minimum amplitude value of the spike, and the fifth datapoints before and after the peaks.

As shown in Fig 3A, the thus constructed comb filters were applied on both the laser noise free and the laser noisy 300–3000 Hz filtered data in order to equally distort the SUA ("spike") waveforms in both cases. Later on, this allowed us to match the features of different spike clusters in the laser free and laser noisy measurements. Since the imaging laser generated artefacts were nonuniform along the electrodes, recordings from different electrodes required filters with custom-set parameters.

We investigated whether the comb filter prevents us from SUA ("spike") detection and sorting. Spike detection was performed by simple thresholding. Three features of each potential spikes were defined for spike sorting, which were the location of the minimum amplitude value of the spike, and the values at 250 microseconds (i.e. five datapoints) before and after the peaks (Fig 5). The clusters were manually accepted or discarded based on spike waveforms and autocorrelograms. This feature extraction method was preferred rather than principal component analysis (PCA), because the thus defined features could provide more robust information about spike waveform consistency (spike stability). In terms of the laser noise free part of the experiments, we performed a comparison of the feature-based and the PCA methods on the band-pass filtered data to verify the results of the feature extraction based method which was used for testing the spike stability too. The spike stability was verified as follows. First, the averages and the standard errors of the means of each feature were calculated in every minute of the recordings. These values were compared to each other during the whole measurement to verify the impact of the imaging laser and the applied filters to the shape of the thus sorted spikes. Furthermore, the number of spikes were counted in every minute of the recordings for each clusters. This method showed whether the artefacts caused by the imaging laser gave rise to false positive SUA detections.

Results and discussion

As shown previously, simultaneous two-photon imaging and electrophysiological measurements with MEMS microelectrode arrays at the same location is compromised by the

formation of photoelectric artefacts in the electrophysiological signals. Regarding our experiments when electrodes were located within the two-photon imaging window, the imaging laser was able to create such artefacts with amplitudes of typically 50 times greater than the amplitude of the largest single unit activities. Moreover, the complicated spectrum of the photoelectric noise prevents the filtering of the artefact via simple filters.

Our following results suggest that the utilization of a comb filter-based algorithm can enable researchers to detect and sort single unit activities even if the tissue surrounding the microelectrode array is observed with two-photon microscopy. Fig 6 illustrates the observed area and suggests that the above described two-photon microscope setup and settings were suitable for detecting activities of neuron somas and dendrites via calcium imaging.

The filters influenced frequency spectrum of the electrophysiological recordings is shown in S1 Fig, where subfigure A shows the absolute value of the frequency spectrum of the unfiltered signal, subfigure B shows the absolute value of the frequency spectrum of the band-pass filtered signal while subfigure C shows the absolute value of the frequency spectrum of the band-pass and noise filtered signal. Comparing the subfigures, it can be observed that after both of the filtering processes the frequency component of the noise became two orders of magnitude lower. Fig 7 shows neural signal samples obtained from an electrode illuminated with direct laser light before (green) and after (red) the application of the filter. It is evident that small amplitude spike-like artefacts are still present on the filtered signal and these spike-like artefacts are synchronized with the period of the laser noise. Fortunately, however, we can also observe that major single unit activity amplitudes exceed the amplitude of these artefacts. The filter was also applied on the signal sections which were recorded when the imaging laser was off so those sections can serve as proper references for single unit activity detection. Moreover, with further developments, the artefact spikes can probably be eliminated with an algorithm which takes into account the synchrony of the artefacts and the laser noise. A limitation of this proposed method is that when a single unit activity coincides with a spike artefact, it is probably also eliminated. However, comparing the width and the density of the laser generated artefacts in time range, this limitation should only affect approximately 8.5% of the signal.
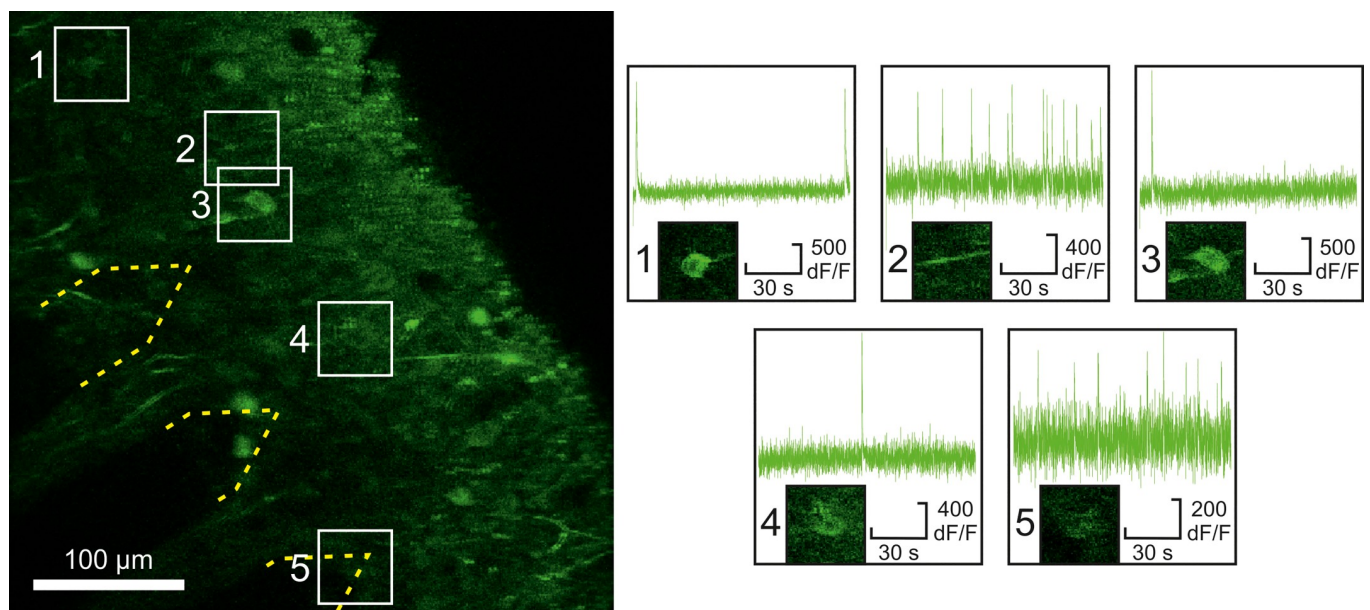

Fig 6. Two-photon calcium imaging. The imaging reveals activities of neuron somas (subfigures 1, 3, 4, 5) and dendrites (subfigure 2) in the vicinity of the microelectrode array.
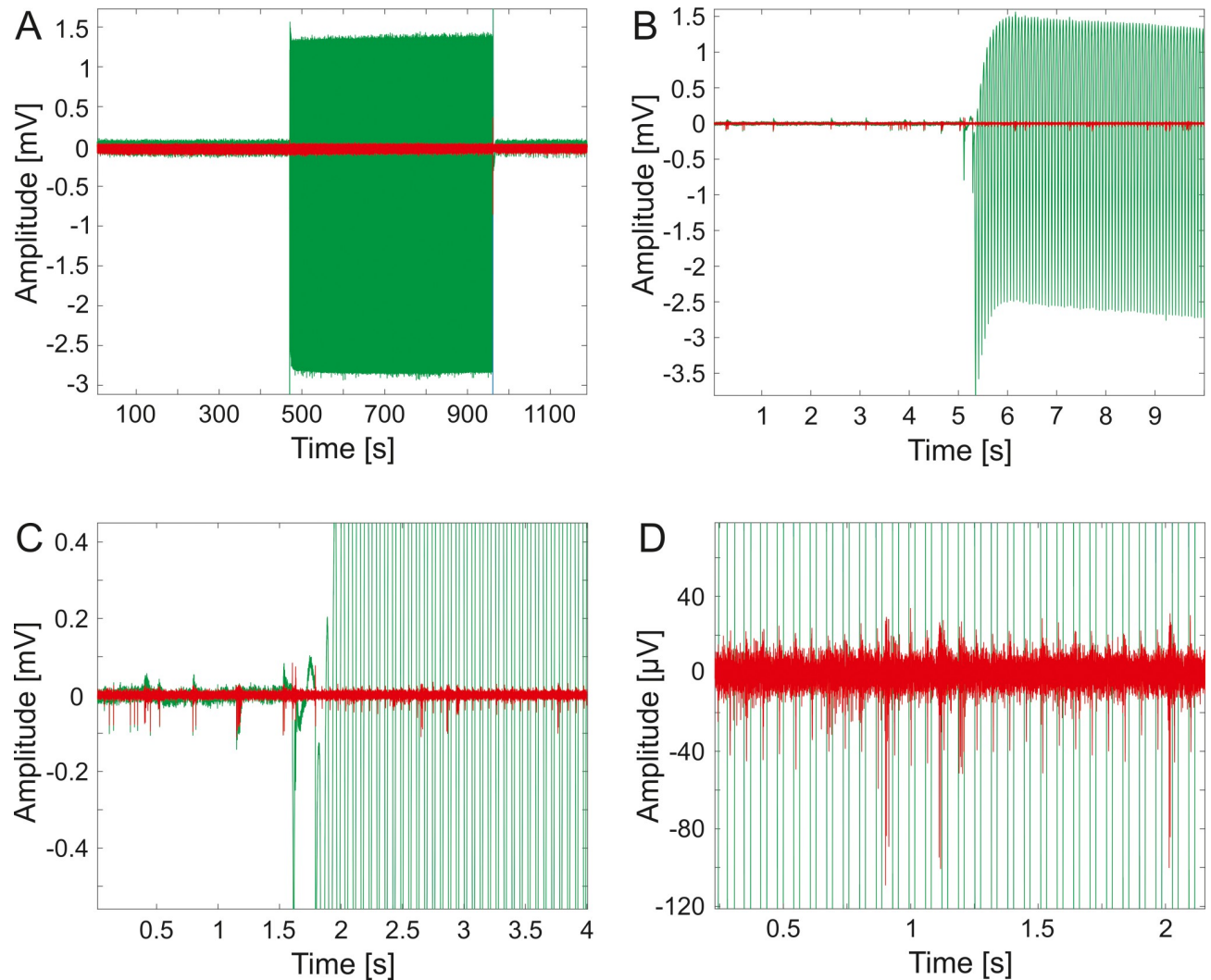
Fig 7. Representative sample of the results of the applied filtering algorithm. The subfigures show the same data as Fig 2 does, prior to filtering (green) and after applying the filtering algorithm (red).

Fig 8A shows the tissue region observed with two-photon microscopy, containing the recording electrode sites. The result of the feature extraction for this representative case is shown in Fig 8B, where the potential spikes are shown in black (detected during the laser off condition) and red (detected during the laser on condition). The obtained spike waveforms, their averages and autocorrelograms in Fig 8C. The differences between the laser on and off conditions are shown in S3 Fig (spike waveforms and their averages) and S4 Fig (autocorrelograms). The results of the comparison of the feature extraction and the PCA based methods for spike sorting is shown in S5 Fig. To verify the applied filtering algorithm, the consistency of the sorted spike waveforms (spike stability) was visualized. Results of the average of spike features within each minute of the recordings suggest that the laser noise does not corrupt the thus obtained spike waveforms (Fig 8D, top). Furthermore, the number of the spikes in each minute of the measurement suggest that the laser noise does not introduce artefact spikes into the clusters (Fig 8D, bottom). A further result is presented in supplementary S2 Fig, which shows a histogram of the occurrence of each spike within the laser noise period. This result
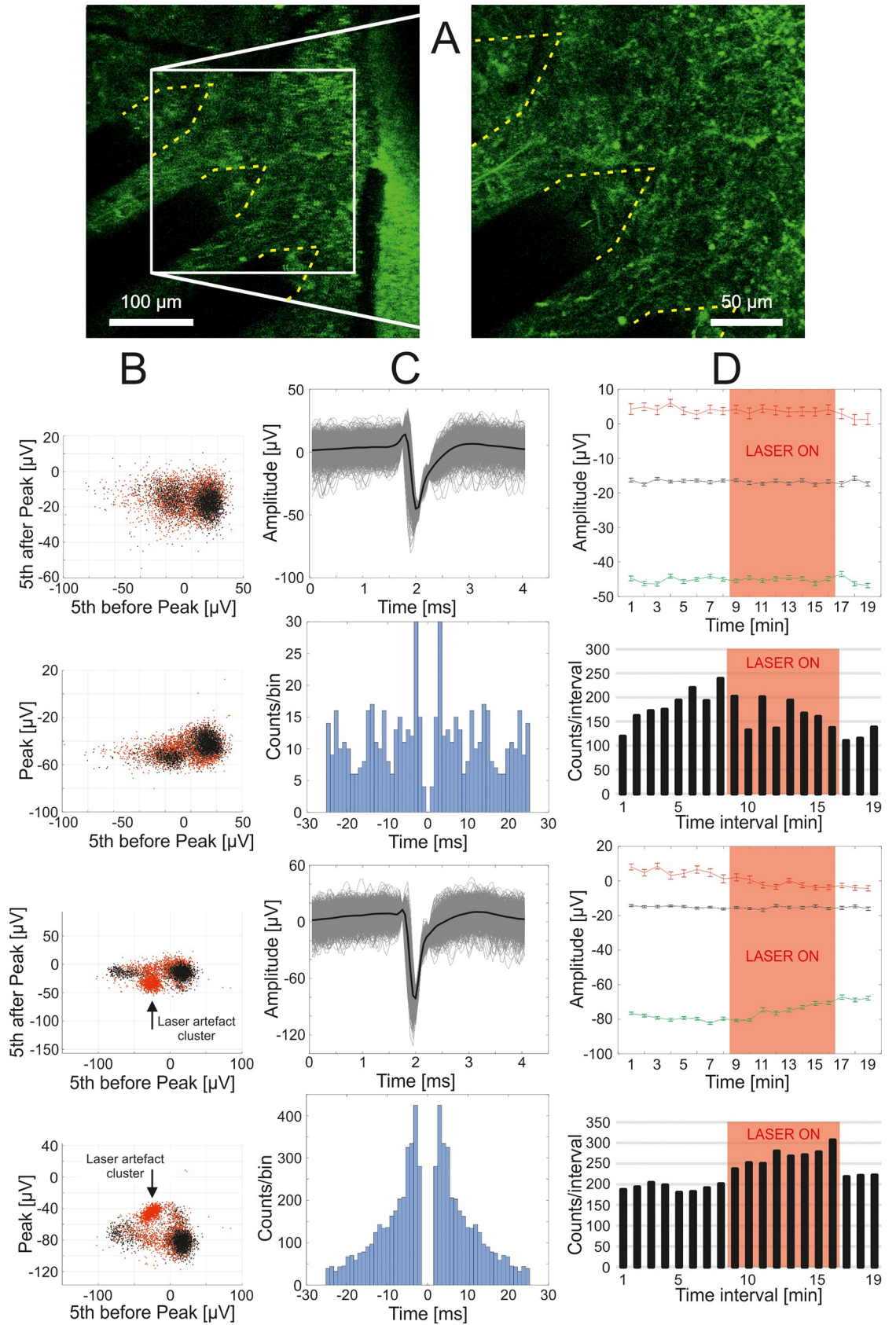
Fig 8. Representative results of the simultaneous measurement of electrophysiological recordings and two-photon imaging. The examined electrodes of the applied MEA were in the two-photon imaging window (A). Two examples of sorted spikes recorded by the electrodes shown in part A (B-D). Potential spikes were sorted using three features obtained from the comb-filtered signals (B). The obtained spike waveforms, their averages (C, top) and the autocorrelograms of the thus sorted spikes (C, bottom). The verification of spike stability during laser noise free and the simultaneous two-photon measurements (containing laser noise) is presented in part D. Changes in the shapes of the detected spikes were observed by comparing the averages and standard errors of spike features during the measurements (D, top). The number of the sorted spikes per minute (D, bottom).

may be caused by modulations of the cells firing rates due to the laser light, as suggested by Kozai et al [43].

We agree with neuroscientists claiming that simultaneous application of two-photon imaging and implanted MEAs would be beneficial for obtaining more complex information about the activity, connectivity and function of brain cells [31,44,45]. One of the major challenges of the simultaneous utilization of these state of the art methods is caused by the photoelectric artifacts on the electrophysiological signals caused by the imaging laser. This challenge was partly overcome previously with various data filtering algorithms [46]. The herein presented filtering method alleviates this hindrance further by offering means for researchers to detect and sort SUAs from recordings infected by the laser noise of a two-photon microscope. However, the methods have still limitations. A "clean", laser noise free recording is suggested to be recorded before and after the actual simultaneous recording in order to verify the validity of the obtained spike features. Furthermore, the applied comb filter distorts spike waveforms more than the more commonly utilized band-stop filters (with cutoff frequencies at e.g. 300 Hz and 3000 Hz). The presented method can be further developed by the application of an automated algorithm which determines the range of the comb filter in the frequency band, and by a more complex software which takes into account the periodicity of the laser noise for spike detection. Some efforts were made for automating the process, i.e. to solve the parameter setting step automatically, but for a sufficiently robust algorithm more work needs to be done on this matter.

Conclusion

In this paper we presented a method for recording extracellular signals with depth microelectrode arrays and two-photon images within the same tissue region, simultaneously, in a such manner that even single unit activities can be obtained from the electrophysiological recordings. To our knowledge, this is the first time that the possibility of obtaining such data has been presented. The applied filtering algorithm was capable of eliminating the majority of the periodic photoelectric artefacts generated by the imaging laser in order to allow us to perform single unit activity detection and sorting. The method might allow researchers to employ two-photon microscopy in order to reveal crucial properties of high density extracellular neurophysiology and vice versa. The application of simultaneous, multimodal measurements might give rise to novel findings in neuroscience and effective brain-computer interfaces.

Supporting information

S1 Fig. The effect of the filters on the frequency spectrum of the electrophysiological recordings. Subfigure A shows the absolute value of the frequency spectrum of the unfiltered signal, subfigure B shows the absolute value of the frequency spectrum of the band-pass filtered signal. Subfigure C shows the absolute value of the frequency spectrum of the band-pass and noise filtered signal.
(TIF)

S2 Fig. The number of the detected neuronal spikes compared to the start of the laser imaging frame acquisition cycle. Subfigures A and B show the occurrence of two sorted spikes presented in Fig 8. It revealed that the firing of the detected cells is modulated with the laser light, as also shown by Kozai et al. [43].
(TIF)

S3 Fig. The detected spike traces and their averages during the laser on and off conditions for two clustered units. The related A-B and C-D subfigures present the first laser off (A and C) and the laser on (B and D) conditions.
(TIF)

S4 Fig. The difference between the autocorrelograms during the laser on and off conditions for two clustered units. The related A-B and C-D subfigures present the first laser off (A and C) and the laser on (B and D) conditions.
(TIF)

S5 Fig. The result of the comparison of two spike sorting methods. The Principal Component Analysis of the laser noise free, band-pass filtered data (A) in the two cases of the presented single unit activities of Fig 8. The detected and sorted SUA waveforms with their averages based on the PCA (B, top) and based on the feature extraction methods (C, top). The interspike interval (ISI) violators based on the PCA (B, bottom) and based on the feature extraction methods (C, bottom).
(TIF)

Acknowledgments

We are grateful to Ms. Jusztina Béres for her assistance in the in vitro experiments.

Author Contributions

Conceptualization: Gábor Orbán, Domokos Meszéna, Kinga Réka Tasnády, István Ulbert, Gergely Márton.

Formal analysis: Gábor Orbán.

Investigation: Gábor Orbán, Domokos Meszéna, Kinga Réka Tasnády.

Methodology: Gábor Orbán, Domokos Meszéna, Gergely Márton.

Resources: István Ulbert, Gergely Márton.

Supervision: István Ulbert, Gergely Márton.

Visualization: Gábor Orbán.

Writing – original draft: Gábor Orbán.

Writing – review & editing: Domokos Meszéna, Balázs Rózsa, Gergely Márton.

References

1. Edelman BJ, Baxter B, He B. No TitleEEG Source Imaging Enhances the Decoding of Complex Right-Hand Motor Imagery Tasks. IEEE Trans Biomed Eng. 2016; 63(1):4–14. https://doi.org/10.1109/TBME.2015.2467312 PMID: 26276986

2. Hochberg LR, Bacher D, Jarosiewicz B, Masse NY, Simeral JD, Vogel J, et al. Reach and grasp by people with tetraplegia using a neurally controlled robotic arm. Nature. 2012; 485:372–5. https://doi.org/10.1038/nature11076 PMID: 22596161

3. Hotson G, McMullen DP, Fifer MS, Johannes MS, Katyal KD, Para MP, et al. Individual finger control of a modular prosthetic limb using high-density electrocorticography in a human subject. J Neural Eng. 2016; 13(2):26017. https://doi.org/10.1088/1741-2560/13/2/026017 PMID: 26863276

4. Schwartz AB, Cui TX, Weber DJ, Moran DW. Brain-Controlled Interfaces: Movement Restoration with Neural Prosthetics. Neuron. 2006; 52(1):205–20. https://doi.org/10.1016/j.neuron.2006.09.019 PMID: 17015237

5. Márton G, Orbán G, Kiss M, Fiáth R, Pongrácz A, Ulbert I. A Multimodal, SU-8—Platinum—Polyimide Microelectrode Array for Chronic In Vivo Neurophysiology. PLoS One. 2015; 10(12). https://doi.org/10.1371/journal.pone.0145307 PMID: 26683306

6. Fiáth R, Raducanu BC, Musa S, Andrei A, Lopez CM, Hoof C van, et al. A silicon-based neural probe with densely-packed low-impedance titanium nitride microelectrodes for ultrahigh-resolution in vivo recordings. Biosens Bioelectron. 2018; 106:86–92. https://doi.org/10.1016/j.bios.2018.01.060 PMID: 29414094

7. Schölvinck ML, Leopold DA, Brookes MJ, Khader PH. The contribution of electrophysiology to functional connectivity mapping. Neuroimage. 2013; 80:297–306. https://doi.org/10.1016/j.neuroimage.2013.04.010 PMID: 23587686

8. Konrad P, Shanks T. Implantable brain computer interface: Challenges to neurotechnology translation. Neurobiol Dis. 2010; 38(3):369–75. https://doi.org/10.1016/j.nbd.2009.12.007 PMID: 20035870

9. Ito S, Yeh F-C, Hiolski E, Rydygier P, Gunning DE, Hottowy P, et al. Large-Scale, High-Resolution Multielectrode-Array Recording Depicts Functional Network Differences of Cortical and Hippocampal Cultures. PLoS One. 2014; 9(8). https://doi.org/10.1371/journal.pone.0105324 PMID: 25126851

10. Neto JP, Lopes G, Frazão J, Nogueira J, Lacerda P, Baião P, et al. Validating silicon polytrodes with paired juxtacellular recordings: method and dataset. J Neurophysiol. 2016; 116(2):892–903. https://doi.org/10.1152/jn.00103.2016 PMID: 27306671

11. Barrese JC, Rao N, Paroo K, Triebwasser C, Vargas-Irwin C, Franquemont L, et al. Failure mode analysis of silicon-based intracortical microelectrode arrays in non-human primates. J Neural Eng. 2013; 10(6):66014. https://doi.org/10.1088/1741-2560/10/6/066014 PMID: 24216311

12. Rousche PJ, Normann RA. Chronic recording capability of the Utah Intracortical Electrode Array in cat sensory cortex. J Neurosci Methods. 1998; 82(1):1–15. https://doi.org/10.1016/S0165-0270(98)00031-4 PMID: 10223510

13. Kozai TDY, Jaquins-Gerstl AS, Vazquez AL, Michael AC, Cui XT. Brain Tissue Responses to Neural Implants Impact Signal Sensitivity and Intervention Strategies. ACS Chem Neurosci. 2015; 6(1):48–67. https://doi.org/10.1021/cn500256e PMID: 25546652

14. Gilgunn PJ, O. XC, Flesher SN, Schwartz AB, Gaunt RA. Structural analysis of explanted microelectrode arrays. In: Neural Engineering (NER), 2013 6th International IEEE/EMBS Conference. 2013. p. 719–22.

15. Kozai TDY, Catt K, Li X, Gugel Z V., Olaffson VT, Vazquez AL, et al. Mechanical failure modes of chronically implanted planar silicon-based neural probes for laminar recording. Biomaterials. 2015; 37:25–39. https://doi.org/10.1016/j.biomaterials.2014.10.040 PMID: 25453935

16. Karumbaiah L, Norman SE, Rajan NB, Anand S, Saxena T, Betancur M, et al. The upregulation of specific interleukin (IL) receptor antagonists and paradoxical enhancement of neuronal apoptosis due to electrode induced strain and brain micromotion. Biomaterials. 2012; 33(26):5983–96. https://doi.org/10.1016/j.biomaterials.2012.05.021 PMID: 22681976

17. Polikov VS, Tresco PA, Reichert WM. Response of brain tissue to chronically implanted neural electrodes. J Neurosci Methods. 2005; 148(1):1–18. https://doi.org/10.1016/j.jneumeth.2005.08.015 PMID: 16198003

18. Prasad A, Xue QS, Sankar V, Nishida T, Shaw G, Streit WJ, et al. Comprehensive characterization and failure modes of tungsten microwire arrays in chronic neural implants. J Neural Eng. 2012; 9(5):56015. https://doi.org/10.1088/1741-2560/9/5/056015 PMID: 23010756

19. Hillman EMC. Optical brain imaging in vivo: techniques and applications from animal to man. J Biomed Opt. 2007; 12(5):51402. https://doi.org/10.1117/1.2789693 PMID: 17994863

20. Fiala A, Suska A, Schlüter OM. Optogenetic Approaches in Neuroscience. Curr Biol. 2010; 20(20):R897–R903. https://doi.org/10.1016/j.cub.2010.08.053 PMID: 20971436

21. So PTC, Dong CY, Masters BR, Berland KM. Two-photon excitation fluorescence microscopy. Annu Rev Biomed Eng. 2000; 2:399–429. https://doi.org/10.1146/annurev.bioeng.2.1.399 PMID: 11701518

22. Bertrán MA, Martínez NL, Wang Y, Dunson D, Sapiro G, Ringach D. Active learning of cortical connectivity from two-photon imaging data. PLoS One. 2018; 13(5). https://doi.org/10.1371/journal.pone.0196527 PMID: 29718955

23. Bass C, Helkkula P, Paola V De, Clopath C, Bharath AA. Detection of axonal synapses in 3D two-photon images. PLoS One. 2017; 12(9). https://doi.org/10.1371/journal.pone.0183309 PMID: 28873436

24. Kerr JND, Greenberg DS, Helmchen F. Imaging input and output of neocortical networks in vivo. Proc Natl Acad Sci U S A. 2005; 102(39):14063–8. https://doi.org/10.1073/pnas.0506029102 PMID: 16157876

25. Kerr JND, de Kock CPJ, Greenberg DS, Bruno RM, Sakmann B, Helmchen F. Spatial Organization of Neuronal Population Responses in Layer 2/3 of Rat Barrel Cortex. J Neurosci. 2007; 27(48):13316–28. https://doi.org/10.1523/JNEUROSCI.2210-07.2007 PMID: 18045926

26. Stosiek C, Garaschuk O, Holthoff K, Konnerth A. In vivo two-photon calcium imaging of neuronal networks. Proc Natl Acad Sci U S A. 2003; 100(12):7319–24. https://doi.org/10.1073/pnas.1232232100 PMID: 12777621

27. Malik WQ, Schummers J, Sur M, Brown EN. Denoising Two-Photon Calcium Imaging Data. PLoS One. 2011; 6(6). https://doi.org/10.1371/journal.pone.0020490 PMID: 21687727

28. Pacheco S, Wang C, Chawla MK, Nguyen M, Baggett BK, Utzinger U, et al. High resolution, high speed, long working distance, large field of view confocal fluorescence microscope. Sci Rep. 2017; 7 (1):2045–322. https://doi.org/10.1038/s41598-017-01960-5

29. Kozai TDY, Eles JR, Vazquez AL, Cui TX. Two-photon imaging of chronically implanted neural electrodes: Sealing methods and new insights. J Neurosci Methods. 2016; 258:46–55. https://doi.org/10.1016/j.jneumeth.2015.10.007 PMID: 26526459

30. Kuzum D, Takano H, Shim E, Reed JC, Juul H., Richardson AG, et al. Transparent and flexible low noise graphene electrodes for simultaneous electrophysiology and neuroimaging. Nat Commun. 2014; 20(5):5259. https://doi.org/10.1038/ncomms6259 PMID: 25327632

31. Kozai TDY, Vazquez AL. Photoelectric artefact from optogenetics and imaging on microelectrodes and bioelectronics: new challenges and opportunities. J Mater Chem B. 2015; 3(25):4935–5124. https://doi.org/10.1039/c5tb00108k PMID: 26167283

32. Zhang T, Okada Y. Recursive artifact windowed–single tone extraction method (RAW–STEM) as periodic noise filter for electrophysiological signals with interfering transients. J Neurosci Methods. 2006; 155:308–318. https://doi.org/10.1016/j.jneumeth.2005.12.022 PMID: 16466806

33. Prance H, Prance RJ, Stiffell PB. Hardware comb filter enhances dynamic range and noise performance of sensors in noisy environments. Rev Sci Instrum. 2007; 78(074701). https://doi.org/10.1063/1.2751399 PMID: 17672781

34. Materka A, Byczuk M. Using comb filter to enhance SSVEP for BCI applications. In: 3rd Int Conf MED-SIP 2006, Advances in Medical, Signal and Information Processing, Glasgow. 2006.

35. Chabuda A, Durka P, Zygierewicz J. High Frequency SSVEP-BCI With Hardware Stimuli Control and Phase- Synchronized Comb Filter. IEEE Trans Neural Syst Rehabil Eng. 2018; 26(2). https://doi.org/10.1109/TNSRE.2017.2734164 PMID: 28961117

36. Wu V, Barbash IM, Ratnayaka K, Saikus CE, Sonmez M, Kocaturk O, et al. Adaptive Noise Cancellation to Suppress Electrocardiography Artifacts During Real-Time Interventional MRI. J Magn Reson Imaging. 2011; 33:1184–1193. https://doi.org/10.1002/jmri.22530 PMID: 21509878

37. Kockanat S, Kockanat S. Analysis and Extraction of Fetal Electrocardiogram Signal with Adaptive Filtering Using Differential Evolution Algorithm. Cumhur Sci J. 2018; 39(1):294–302. https://doi.org/10.17776/csj.407424

38. Dana H, Chen T-W, Hu A, Shields BC, Guo C, Looger LL, et al. Thy1-GCaMP6 Transgenic Mice for Neuronal Population Imaging In Vivo. PLoS One. 2014; 9(9):108697. https://doi.org/10.1371/journal.pone.0108697 PMID: 25250714

39. Wertz A, Trenholm S, Yonehara K, Hillier D, Raics Z, Leinweber M, et al. Single-cell–initiated monosynaptic tracing reveals layer-specific cortical network modules. Science (80-). 2015; 349(6243):70–4. https://doi.org/10.1126/science.aab1687 PMID: 26138975

40. Grand L, Pongrácz A, Vázsonyi É, Márton G, Gubán D, Fiáth R, et al. A novel multisite silicon probe for high quality laminar neural recordings. Sensors Actuators A Phys. 2011; 166(1):14–21. https://doi.org/10.1016/j.sna.2010.12.019

41. Hájos N, Ellender TJ, Zemankovics R, Mann EO, Exley R, Cragg SJ, et al. Maintaining network activity in submerged hippocampal slices: importance of oxygen supply. Eur J Neurosci. 2009; 29(2):319–327. https://doi.org/10.1111/j.1460-9568.2008.06577.x PMID: 19200237

42. Quiroga RQ, Nadasdy Z, Ben-Shaul Y. Unsupervised Spike Detection and Sorting with Wavelets and Superparamagnetic Clustering. Neural Comput. 2004; 16(8):1661–87. https://doi.org/10.1162/089976604774201631 PMID: 15228749

43. Stocking KC, Vazquez AL, Kozai TDY. Intracortical neural stimulation with untethered, ultrasmall carbon fiber electrodes mediated by the photoelectric effect. IEEE Trans Biomed Eng. 2019; https://doi.org/10.1109/TBME.2018.2889832 PMID: 30605086

44. Qiang Y, Artoni P, Seo KJ, Culaclii S, Hogan V, Zhao X, et al. Transparent arrays of bilayer-nanomesh microelectrodes for simultaneous electrophysiology and two-photon imaging in the brain. Sci Adv. 2018; 4(9):eaat0626. https://doi.org/10.1126/sciadv.aat0626 PMID: 30191176

45. Park D-W, Brodnick SK, Ness JP, Atry F, Krugner-Higby L, Sandberg A, et al. Fabrication and utility of a transparent graphene neural electrode array for electrophysiology, in vivo imaging, and optogenetics. Nat Protoc. 2016; 11:2201–22. https://doi.org/10.1038/nprot.2016.127 PMID: 27735935

46. Shew WL, Bellay T, Plenz D. Simultaneous multi-electrode array recording and two-photon calcium imaging of neural activity. J Neurosci Methods. 2010; 192:75–82. https://doi.org/10.1016/j.jneumeth.2010.07.023 PMID: 20659501